ELSEVIER

Dynamics of Atmospheres and Oceans
36 (2002) 153–173

dynamics of atmospheres and oceans

www.elsevier.com/locate/dynatmoce

The influence of the coast on the dynamics of upwelling fronts Part I. Laboratory experiments

Pascale Bouruet-Aubertot [a,*], P.F. Linden [b]

[a] *D.A.M.T.P., University of Cambridge, Silver Street, Cambridge CB93EW, UK*
[b] *Department of Mechanical and Aerospace Engineering, University of California, San Diego, 9500 Gilman Drive La Jolla, CA 92093-0411, USA*

Received 12 September 2000; received in revised form 23 January 2002; accepted 25 March 2002

Abstract

We describe laboratory experiments on the instability and later evolution of a front in a two-layer rotating fluid. In particular, we focus on the influence of a nearby boundary on instability growth and eddy formation. The front is produced through the adjustment of a buoyant fluid initially confined within a bottomless cylinder. Typically a front in quasi-cyclostrophic balance establishes after two rotation periods, after which it becomes unstable. Measurements of the velocity and vorticity fields at the surface are made which provide detailed information on the evolution of the front as the instability grows to finite amplitude. We focus on the time evolution of the vorticity and distinguish between the cyclonic and anticyclonic components. The spatial averages of the cyclonic and anticyclonic vorticity first grow exponentially. This growth saturates when eddies form and are advected across the front. The growth rate depends upon two nondimensional parameters: the width W of the upwelling region in units of the internal radius of deformation and the depth ratio δ between the two layers. Measurements of the growth rates for the average of the cyclonic and anticyclonic vorticity are compared to the values inferred from a simplified model for baroclinic instability. A good agreement is obtained when the front develops far from the boundary (i.e. $W \gg 1$). However, the agreement is only qualitative when the front is near the boundary (i.e. $W \sim 1$). We find that, as W decreases, the growth of cyclonic eddies consisting of dense—"coastal"—water is enhanced compared to that of anticyclonic vorticity consisting of buoyant—"off-shore"—water. This crucial effect of the boundary with respect to the instability of the front has significant impact on exchanges across the front.

Keywords: Influence of the coast; Dynamics of upwelling fronts; Laboratory experiments

* Corresponding author. Present address: LODYC, U. Pierre et Marie Curie/UMR 7617 CNRS/IRD/UPMC, 4 place Jussieu, 75252 Paris Cedex 05, France.
E-mail address: pascale.bouruet-aubertot@lodyc.jussieu.fr (P. Bouruet-Aubertot).

0377-0265/02/$ – see front matter
PII: S0377-0265(02)00029-5

1. Introduction

The experiments presented in this paper aim to improve understanding of physical processes involved in the dynamics of oceanic fronts. Fronts are regions of large gradients of physical and chemical properties and dynamical features and constitute a transition between two water masses. There is often a significant density gradient across the front, in which case a steady state, with an along-front current in geostrophic equilibrium, can be reached. As a consequence water exchanges can only occur through the instability of the front which leads to meanders, filaments and eddies (Gill et al., 1974). A common form of front can occur as a result of upwelling, with a density gradient at the surface between deeper cold water and warmer off-shore surface waters. For instance the upwelling front off California and Oregon shows a complex structure of meanders, eddies and filaments along the length of the current (Ikeda and Emery, 1984; Flament et al., 1985; Strub et al., 1991; Ramp et al., 1991). Fronts are also associated with buoyancy-driven coastal currents that flow along the coast. These fronts show wave-like meanders as, for instance, the Leeuwin current which flows poleward along the western coast of Australia (Pearce and Griffiths, 1991). Low frequency meanders of a warm coastal current in the Ligurian Sea have been observed (Crépon et al., 1982). These wavy patterns have been interpreted in terms of large amplitude baroclinic waves using a two-layer model for baroclinic instability, and the observed wavelength of about 38 km is fairly close to the theoretically most unstable wavelength of about 48 km.

Laboratory experiments to investigate the instability of either coastal current or upwelling fronts have been performed (for a review, Linden, 1991). These fronts were produced in the laboratory in a two-layer stratification using two different methods. In the first method, referred to as “constant flux experiments”, the front is produced by releasing some dyed buoyant fluid at the surface of a denser fluid. The buoyant fluid was released along a circular ring that encloses a vertical cylinder, the analogue of the coast (Griffiths and Linden 1981a,b; Cenedese, 1998). In these experiments, the marginal flow stability is analysed as well as the subsequent instability. Alternatively, the front is produced through the adjustment of a buoyant patch of fluid initially confined within an inner bottomless cylinder (Griffiths and Linden, 1981a, 1982; Chia et al., 1982; Holford and Dalziel, 1996). These experiments are generally referred to as “constant volume experiments” and focus upon the instability of supercritical flows.

The main difference between coastal currents and upwelling fronts comes from the shape of the interface between the two water masses. In the former, the interface slopes downward from the front to the boundary. For an upwelling front, the interface slopes upward toward the vertical boundary. Therefore, provided that the instability of the front develops sufficiently far from the boundary, no significant difference in behaviour is observed. On the other hand, when the front is close to the boundary, we expect to observe different behaviour in the two cases.

Previous laboratory experiments have shown that the nature of the instability depends on the width of the current or the radius of the buoyant patch in units of the radius of deformation. When this dimensionless width is small, the instability is primarily barotropic and driven by the horizontal shear, while when it is large, the instability is predominantly baroclinic, driven by the vertical shear in the horizontal current. The depth ratio between

the two layers influences the critical width for the transition between these two kinds of instabilities (Griffiths and Linden, 1981b).

In both cases, whether marginally stable or supercritical, the instability takes the form of azimuthal waves (Linden, 1991). The circulation is anticyclonic at the wave crests while cyclonic vorticity grows at the wave troughs. For sufficiently large amplitude, these waves eventually break leading to the formation of vortex-dipoles consisting of an anticyclonic eddy of buoyant fluid and a cyclonic eddy of denser fluid surrounded by buoyant fluid (Griffiths and Linden, 1981a,b, 1982; Holford, 1994; Holford and Dalziel, 1996). In some cases, when fronts are free of the effects of friction, these eddy dipoles detach from the front and self-propagate (Holford, 1994). These features are common to both coastal currents and upwelling fronts provided that the instability develops far from the outer boundary though their velocity profiles and potential vorticity distributions differ. The influence of the outer vertical boundary was investigated by Chia et al. (1982). Cyclonic eddies containing coastal water were observed to intensify when the instability of the front develops near the boundary.

Quantitative results obtained previously mainly concern the wavelength of the instability and this quantity has provided the basis for comparison with theoretical predictions. The most simplified model for baroclinic instability is that of a two-layer fluid in a channel having uniform velocities in each layer (Phillips, 1954). The wavelength λ of the most unstable mode scales with the geometric mean of the radii of deformation of the two layers, $\mathrm{Rd}_{\mathrm{mean}}$: $\lambda = 1.08(2\pi)\mathrm{Rd}_{\mathrm{mean}}$. Killworth et al. (1984) show that when the interface outcrops at the surface, instability occurs for any spatial variation of the potential vorticity. Two kinds of perturbations are obtained: a long wavelength instability which is of mixed barotropic-baroclinic nature, and a short-wave barotropic instability. Barotropic effects dominate when the width of the current is smaller than the radius of deformation while baroclinic effects dominate for wider currents, consistently with previous laboratory experiments (Griffiths and Linden, 1982). Killworth et al. (1984) also applied their model to a situation closer to that of Phillips in order to estimate the contribution of ageostrophic effects. They found that the most unstable wavelength is fairly close to that given by Phillips' model: $\lambda = 1.15(2\pi)\mathrm{Rd}_{\mathrm{mean}}$. However, they found a significant difference in growth rate, which was smaller by a factor of 7 than that obtained from quasi-geostrophic theory. These differences may also result from the different assumptions for the lower layer flow and from different boundary conditions. Verzicco et al. (1997) performed direct numerical simulations to reproduce the evolution of a baroclinic vortex, similar in shape to that studied experimentally by Griffiths and Linden (1981a), and Holford (1994). They showed that the instability of the vortex is initially driven by the baroclinic term whatever the value of the depth ratio. Good agreement with laboratory experiments was obtained regarding the wavelength of the dominant unstable mode.

We report new laboratory experiments on a front in a two-layer fluid and with background rotation. In the experiments, the front is produced using the Rossby adjustment method (Chia et al., 1982). The buoyant patch is initially confined to a circular region so that the shape of the resultant front is similar to that of an upwelling front in which the interface depth decreases toward the coast. The laboratory experiments focus on the instability of the front and the subsequent formation of eddy structures that contribute to exchanges across the front. The aim of the experiments, which are a replication of the experiments performed by Chia et al. (1982), is to give further insights on the influence of the outer boundary upon

these processes. In particular, we describe a quantitative analysis of the instability inferred from the analysis of surface velocity and vorticity fields.

In Section 2, we describe the experiments and give the range of parameters considered. We give an overview of the evolution of the front in Section 3. A detailed analysis of the dynamics governing the establishment of the front and its instability is presented in Section 4 where growth rates of the instability are inferred from the time evolution of surface vorticity fields and compared with simplified theories for baroclinic instability. Conclusions are given in Section 5.

2. The experiments

The upwelling front is produced through the adjustment of a buoyant fluid that is initially confined within a bottomless cylinder in a similar manner to that of Chia et al. (1982). The experimental set-up is displayed in Fig. 1. A tank of radius $R = 37$ cm was used and the inner cylinder diameter was of radius $R_c = 27$ cm; the turntable rotated at an angular velocity Ω, corresponding to a Coriolis parameter $f = 2\,\Omega$.

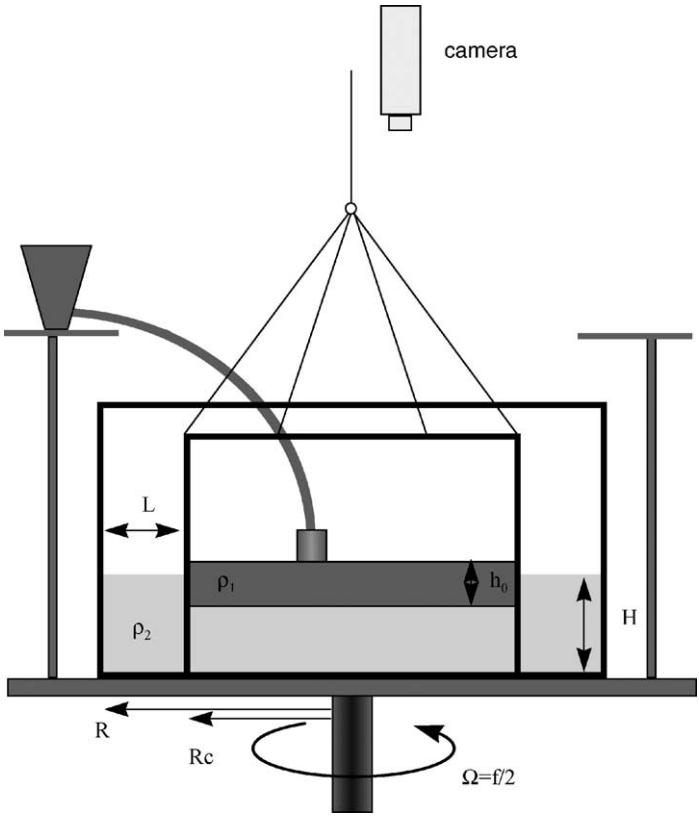

Fig. 1. Experimental set-up (see text for details).

The experimental procedure consists of three stages. The tank was first filled with salt solution of density ρ_2 to a prescribed depth H, and spun up to solid body rotation. Fresh water of density ρ_1 was then carefully released at the surface within the inner cylinder until the required depth h_0 is reached. The fresh water was dyed for flow visualization. The system was then left to spin up to solid-body rotation. The experiment was initiated by the withdrawal of the bottomless cylinder: the two layers adjust under the influence of buoyancy and Coriolis forces. Typically a front in quasi-cyclostrophic balance was established after about two rotation periods (e.g. Fig. 3a), after which it became unstable.

The experiments were recorded onto a video tape recorder using a video camera. Detailed measurements of the velocity and vorticity at the surface were obtained from particle tracking. A computer system with a frame-grabber and the image processing *DigImage* (Dalziel, 1992) was used to acquire and process the images from the video records. Particles were placed in the flow at the surface just before the withdrawal of the bottomless cylinder. Usually the particles were paper pellets (of diameter of about 0.5 cm), which do not require any particular lighting conditions and allows the front to be tracked simultaneously by observing the dyed buoyant water. However, due to the particle size, it was necessary to determine whether drag effects were significant. Consequently, we performed similar experiments but introduced much smaller particles (of Pliolite type having a diameter of about 600 μm) in the flow, illuminated by a horizontal light sheet. Excellent agreement between the measurements inferred from both kinds of particles was obtained. Typically, a few hundred (less than 500) particles are located in each frame and the velocities are obtained by sampling the video film at a frequency of 25 Hz. Automatic matching of particle locations from frame to frame produces the tracking files. Particle velocities are calculated over three frames and the velocity field is obtained by mapping the individual velocity vectors onto a rectangular grid. The spatial averaging is performed using a Gaussian window with width chosen as a function of the radius of deformation of the upper layer: $\mathrm{Rd} = (g'h_0)^{1/2}/f$ where $g' = g(\rho_2 - \rho_1)/\rho_2$ is the reduced gravity. The window was usually of about 1.5Rd, and temporal averaging over typically 0.12 s was performed. The vorticity was calculated from the gridded velocity data. The error in the velocities is estimated to be less than 5% (Linden et al., 1995), whereas the error in the vorticity field is about 10%.

Two main dimensionless parameters, the nondimensional width of the upwelling region $W = (R - R_c)/\mathrm{Rd}$ and the depth ratio $\delta = h_0/H$ describe the flow. The effect of the

Table 1
Parameters of the experiments presented in the figures

Experiment	W^2	δ	f (rad/s)	Rd (cm)	H (cm)	h_0 (cm)	g'(cm/s^2)
Exp1	36	0.48	2	1.65	14.9	7.14	1.52
Exp2	8.28	1.08	2	3.47	9	9.76	4.94
Exp3	3.96	1	2	5.02	8.8	8.8	11.43
Exp4	3.83	0.52	4	5.10	9	4.69	88.9

$W^2 = [(R - R_c)/\mathrm{Rd}]^2$ characterises the proximity of the front from the vertical boundary, δ the depth ratio, f the Coriolis parameter, Rd the radius of deformation of the buoyant patch, H the initial depth of the lower layer fluid, h_0 the initial depth of the buoyant fluid and g' is the reduced gravity. The range of variations of the variables are the following: W^2 (0.24–36), δ (0.06–1.02), f (1–4), $\mathrm{Rd} = (g'h_0)^{1/2}/f$ (1.65–20.45), H (6.9–14.9), h_0 (3–10), $g' = 2(\rho_2 - \rho_1)/(\rho_2 + \rho_1)g$ (6.9–137).

proximity of the coast to the front is given by W; small values occur when the front is close to the coast. Note that in these experiments $(\mathrm{Rd}/R_c)^2$ was always small [within $(3 \times 10^{-3}; 6 \times 10^{-2})$] so that baroclinic instability dominates (Griffiths and Linden, 1981a). Also we find that the effects of friction are small and we will neglect them in the further discussion.

In the experiments, the rotation rate f, the density difference between the two layers, the depth H of the fluid and the upper layer depth h_0 are varied. Parameters of the experiments described in detail are given in Table 1.

3. Overview of the flow evolution

Typically a front establishes when $W > 1$. Figs. 2 and 3 show examples of the evolution for two values of W ($W^2 \sim 36$ and $W^2 \sim 8$, respectively). An example of the evolution of surface velocity and vorticity fields is shown in Fig. 4 for $W^2 \sim 4$. Velocity vectors are represented by arrows and the vorticity by a colour scale in which blue corresponds to anticyclonic vorticity and yellow to cyclonic vorticity.

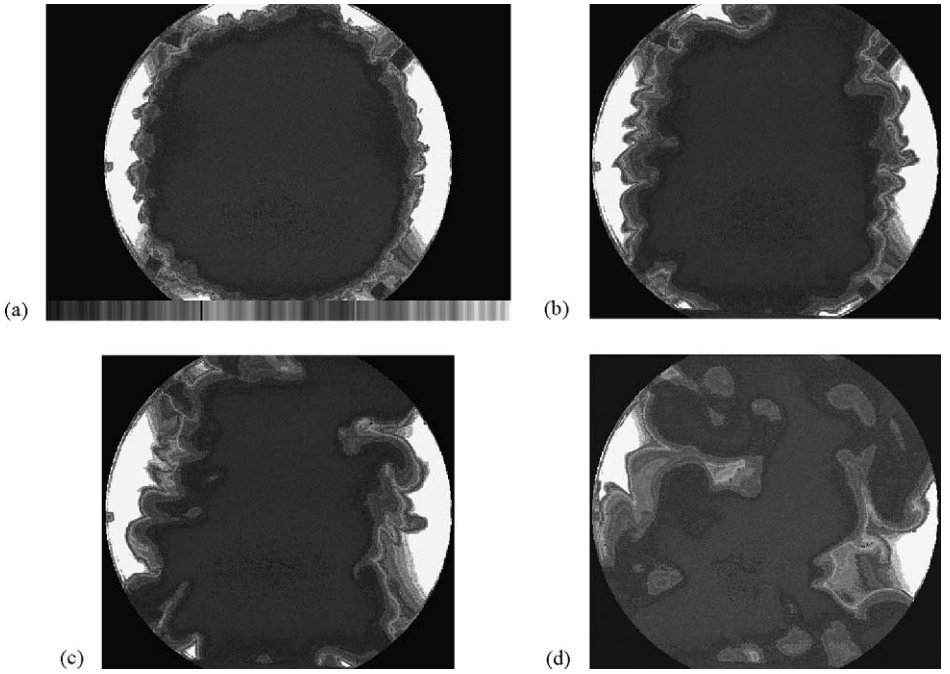

Fig. 2. Overview of the evolution of the front for $W^2 = 36$, $\delta = 0.48$, $f = 2.0$ (Exp1). The fresh water is coloured with some dye to make the front visible (intensity scale is indicated in (a)). Time is indicated in rotation periods, T: (a) at time t_0 after the adjustment when the front is established, small-scale perturbations are also present. (b) At time $t = t_0 + 2.5T$: wave-disturbances are growing. (c) At time $t = t_0 + 6.4T$: same as in (b), but wave disturbance amplitude increases further. (d) At time $t = t_0 + 12.7T$: as the wave amplitude continues to increase, cyclonic eddies of coastal water form and are advected across the front.

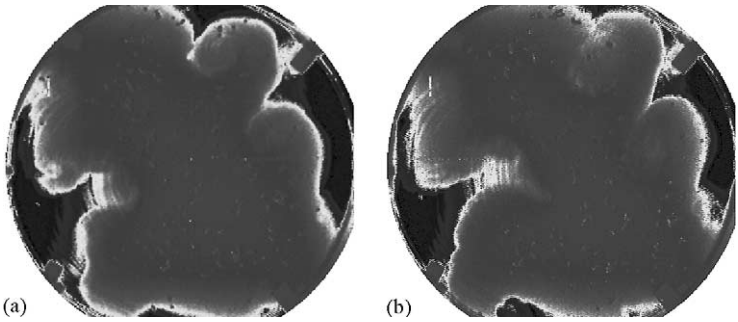

Fig. 3. Overview of the evolution of the front for $W^2 = 8.28$, $\delta = 1.08$, $f = 2.0$ (Exp2). (a) At time $t = t_0 + 3T$: the waves have grown to fairly large amplitude—backward breaking is observed especially in the upper right part. This leads to the formation of vortex dipoles consisting of a cyclonic eddy of lower layer fluid surrounded by upper layer fluid and the anticyclonic part of the wave crest. (b) At time $t = t_0 + 4T$: some of the wave crests have reached the boundaries in the lower part. The wave crest then separates into two branches, one flowing along the boundaries while the other one is flowing away from the boundary (lower left-hand part).

After the withdrawal of the bottomless cylinder, the buoyant fluid spreads radially under the action of the radial pressure gradient. An along-front anticyclonic flow develops until a cyclostrophic balance between the centrifugal force, the Coriolis force and the pressure force is reached after about two rotation periods (Figs. 2a and 4b). During this adjustment process, waves are radiated at the edge of the front and travel along the interface. This process leads to the pulsation of the upper layer as the potential energy released is converted into kinetic energy and conversely (see Section 4.1). The horizontal velocity is thus periodically divergent and convergent with a period slightly larger than $2\pi/f$ (Fig. 4a). The amplitude of these motions is fairly large: the maximum divergence of the horizontal velocity during the adjustment (not shown) is close to the maximum of the vorticity of the flow when the front instability saturates. The vorticity of the buoyant fluid is then mostly anticyclonic except around the edge of the front where the vorticity is cyclonic (Fig. 4b). This horizontal shear produces small-scale perturbations which form rapidly during the initial adjustment (Fig. 2a). Soon after the establishment of an adjusted front perturbations of larger scales start to grow (Figs. 2c, 3a and 4c). The wavelength of these perturbations scales with the radius of deformation: comparison between Figs. 2 and 3 shows that the ratio between the number of wave crests, of about $(15/7) \sim 2$, varies inversely with the ratio between the radii of deformation, of 1/2.

This linear dependency of the wavelength on the radius of deformation is typical of baroclinic instability (Phillips, 1954). The mechanism for the growth of these baroclinic waves has been extensively described in previous experimental studies (Griffiths and Linden, 1981a; Chia et al., 1982). Cyclonic vorticity is induced in the lower layer at the wave troughs where the fluid columns are stretched to replace the collapsing upper layer fluid, while the vorticity is anticyclonic at the wave crests (Fig. 3a, Fig. 4c). The growth of the instability then leads, for sufficiently large-wave amplitude, to closed cyclonic motions of dense water (Figs. 2d, 3a,b and 4d), and closed anticyclones in the upper layer. These vortex pairs can propagate away from the front due to self-advection.

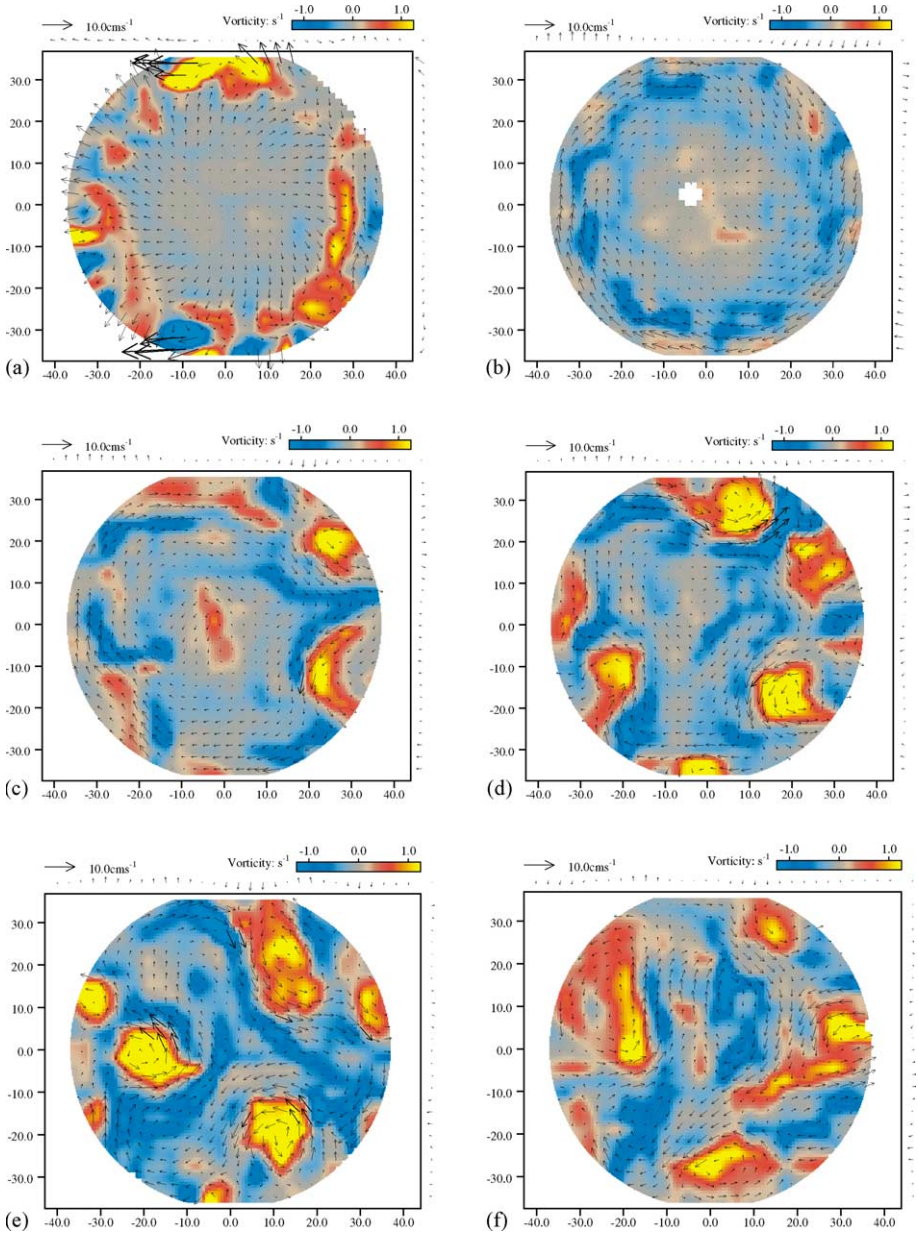

See next page for caption to Fig. 4.

The flow evolves differently depending on the distance between the front and the coast. When the front is far from the boundary (large W), eddy pairs—consisting of a cyclonic eddy made of dense coastal water surrounded by fresh water and an anticyclonic eddy made of upper layer fluid—can form and detach (Griffiths and Linden, 1981a). However, when the wave crests reach the boundary (Figs. 3b and 4d) before the formation of cyclonic eddies an asymmetry between cyclones and anticyclones is observed as previously described by Chia et al. (1982) (see Fig. 6 of their paper). On reaching the boundary, the wave crest spreads in two directions (Fig. 4d). One part spreads upstream and has the boundary on its right and, therefore, flows along the boundary as a buoyancy-driven boundary current. This branch contributes to the enhancement of the cyclonic eddy of dense water induced behind the crest. The other part spreads downstream and is associated with strong off-shore currents which advect cyclonic eddies of dense coastal water across the front toward the centre (Figs. 2d, 3b and 4d,e). The late evolution of the front is characterized by the interaction and decay of large-scale eddies (Fig. 4f).

4. Detailed analysis of the dynamics

4.1. Establishment of the front

Inertial waves are generated after the withdrawal of the inner cylinder (Fig. 5). The waves are generated at the periphery of the buoyant patch where most of the potential energy is released. The waves then propagate away from the front within the stratified area. After the first train of waves reaches the centre of the tank it is radiated back toward the front. The eddy thus pulses between a shallow-wide phase of minimum potential energy to a deep-narrow phase of maximum potential energy. This motion is similar to that described theoretically by Cushman-Roisin et al. (1985) who investigated the oscillations supported by a circular eddy. Similar oscillations have been previously observed in the laboratory experiments by Holford (1994).

Two examples of these waves are shown in Fig. 5, in which the spatial average over the whole domain of the surface velocity is plotted against time for two experiments having

Fig. 4. Surface velocity and vorticity fields for $W^2 = 3.96$, $\delta = 1$, $f = 2.0$ (Exp3). Velocity vectors are represented by arrows and vorticity by the colour scale, in which blue corresponds to anticyclonic vorticity while orange and yellow correspond to cyclonic vorticity. (a) During the adjustment process, inertial waves are radiated and are associated with highly divergent surface velocity. (b) At time $t = t_0$: the front is in quasi-cyclostrophic equilibrium, the circulation in the buoyant layer is anticyclonic and the front is surrounded by a ring of cyclonic vorticity. (c) At time $t = t_0 + 2.5T$: a wave perturbation has grown leading to the development of cyclonic vorticity in the lower layer, situated at the wave troughs, while the vorticity is anticyclonic at the wave crests. (d) At time $t = t_0 + 4T$: cyclonic eddies have formed. Most of the wave crests have reached the boundary. There the wave crest separates into two branches (see especially the two wave crests and neighbouring cyclonic eddies in the upper and lower right-hand part). The upstream branch which flows along the coast leads to the enhancement of the cyclonic eddy behind it while the downstream branch leads to strong off-shore currents. (e) At time $t = t_0 + 6T$: these strong off-shore currents are advecting three of the cyclonic eddies across the front toward the centre. (f) At time $t = t_0 + 12T$: the later evolution is characterized by the interaction and decay of large-scale cyclonic and anticyclonic eddies.

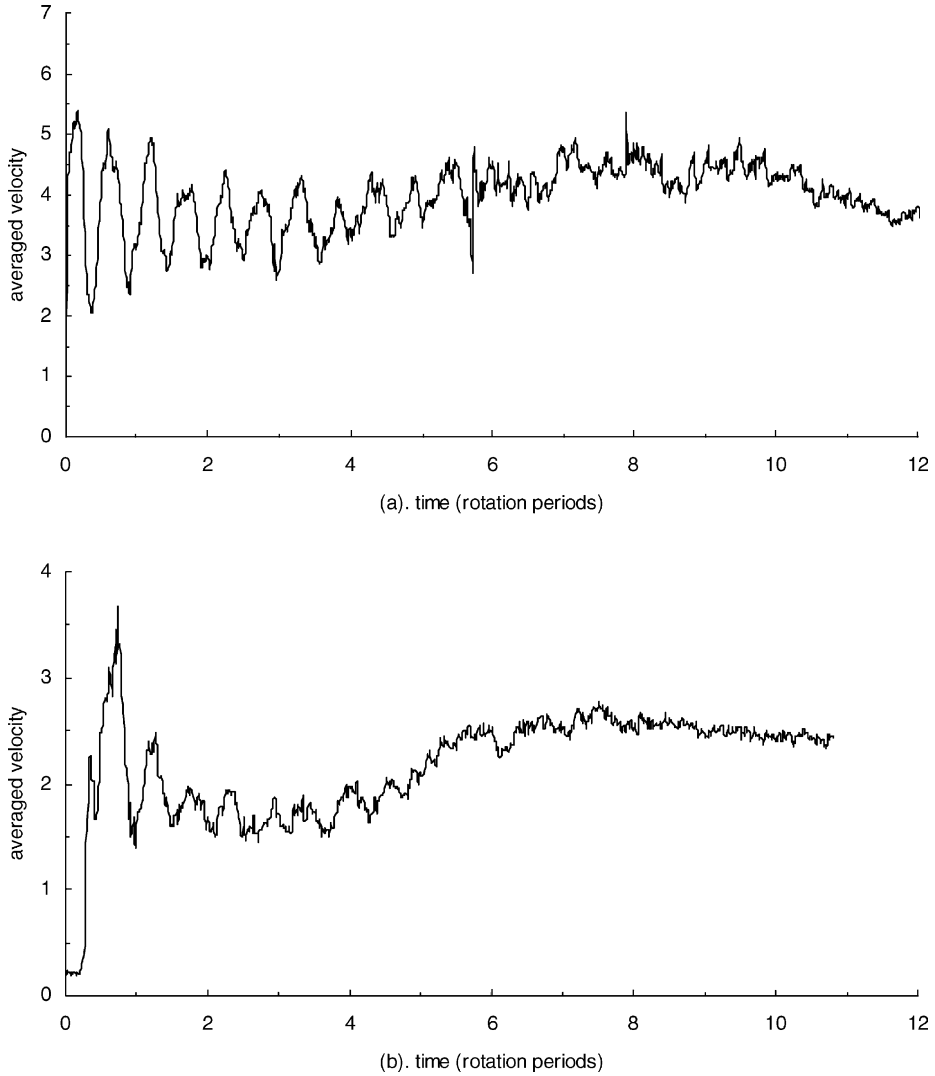

Fig. 5. Inertial oscillations during the adjustment. (a) Spatial average of the modulus of surface horizontal velocity as a function of time for $W^2 = 3.83$, $\delta = 0.52$, $f = 4.0$ rad/s (Exp4). (b) Same as in (a) but for $W^2 = 3.96$, $\delta = 1$, $f = 2.0$ rad/s (Exp3).

same $W^2 = 4$ but different rotation rates $f = 4$ rad/s (Fig. 5a) and $f = 2$ rad/s (Fig. 5b). After the withdrawal of the inner bottomless cylinder, oscillations in the averaged velocity are observed. These oscillations are slightly subinertial of a frequency equal to $0.97f$ (Fig. 5a) and $0.93f$ (Fig. 5b), similar to previous laboratory experiments (Holford, 1994). Numerical simulations of these experiments, Bouruet-Aubertot and Echevin (2002)—hereafter referred to as II, produce subinertial oscillations of kinetic energy and potential energy with

frequency $0.90f$ (see their Fig. 2). It is very likely that the frequency is subinertial because the effective inertial frequency, $f_{\text{eff}} < f$ due to the mean anticyclonic motion: $f_{\text{eff}} = f + \zeta/2$ (Kunze, 1985) where ζ is the relative vorticity. We estimated the frequency shift from the averaged anticyclonic vorticity during the adjustment, and found a frequency shift of the order of 10%, consistent with the values inferred from Fig. 5a and b.

Note that the amplitude of the oscillations is significantly higher in Fig. 5a compared to that in Fig. 5b. The energy of the waves generated during the adjustment is proportional to the potential energy initially available in the system (Gill, 1982). This variation in wave amplitude is consistent with the fact that more potential energy is available in Exp4 than in Exp3 by a factor of about 2. The amplitude of the oscillations decreases exponentially [Fig. 5a (0,3)T, Fig. 5b (0,3)T], and the rate of decay varies with the experiments. For the highest rotation rate, the inertial oscillations are still significant after the onset of baroclinic instability of the front, which results in the growth of the average of the modulus of the surface velocity for $t > 3T$ (Fig. 5a). For the lowest rotation rate, the amplitude of inertial oscillations are only about 10% of the mean "adjusted" flow at $t \sim 2.5T$ (see Fig. 5b). The rate of exponential decrease is smaller, $1.6 \times 10^{-2}\,\text{s}^{-1}$, in (a) compared to the value of $4.7 \times 10^{-2}\,\text{s}^{-1}$ obtained in (b), consistent with the values of the upper-layer Ekman number in (a) (6.5×10^{-9}) compared to (b) (1.1×10^{-8}). As the front becomes unstable some oscillations, having a more complex frequency range, still remain. Note that the instability of the front starts slightly earlier ($t \sim 3T$) in (a) compared to (b) ($t \sim 5T$). It is likely that in the former case, the start of the instability is favoured due to the presence of larger amplitude perturbations. However, the growth rate of the instability is about the same in both cases. The subsequent instability eventually saturates after typically eight rotation periods and a weak decay of the averaged velocity is observed.

We now examine at the radial profile of the mean flow established by the end of the adjustment stage. Our purpose is to determine how these characteristics evolve when the front gets closer to the horizontal boundary. The radial profile of the mean azimuthal surface velocity is displayed in Fig. 6. The buoyant patch extends until $r/\text{Rd} \sim 5.4$ initially and until $r/\text{Rd} \sim 6$. The velocity has a jet-like profile of maximum value near the edge at $r/\text{Rd} \sim 5.8$. The surface vorticity is anticyclonic in the inner side of the front, for $r/\text{Rd} \sim 5.8$ (i.e. in the buoyant upper layer), while it is cyclonic in the outer side of the front, for $r/\text{Rd} \sim 5.8$. The typical width of the shear region is of about 3Rd (Rd $\sim$ 5 cm). Note that the half-width is equal to 1.7Rd. This distance is slightly higher than the spreading distance of the upper layer. The maximum current is of about $0.6c$ (where $c = (g'h_0)^{1/2}$ is the phase speed of internal gravity waves).

The mean azimuthal velocity profile obtained with the same parameters as in the numerical simulations of our experiments (see II) is plotted in Fig. 6. Excellent agreement is obtained. As time increases, this velocity profile starts to be distorted after the onset of baroclinic instability when cyclonic eddies form. Typically the location of the minimum mean azimuthal velocity is shifted toward the centre of the tank (due to the negative azimuthal velocity of cyclonic eddies) while a local maximum in velocity occurs further from the centre (due to the positive azimuthal velocity of cyclonic eddies there). Therefore, when W is fairly high ($W^2 \sim 36$), a double jet can form.

We compare this velocity profile to some theoretical predictions in Fig. 6. There is a qualitative agreement with the most simplified model which assumes conservation of

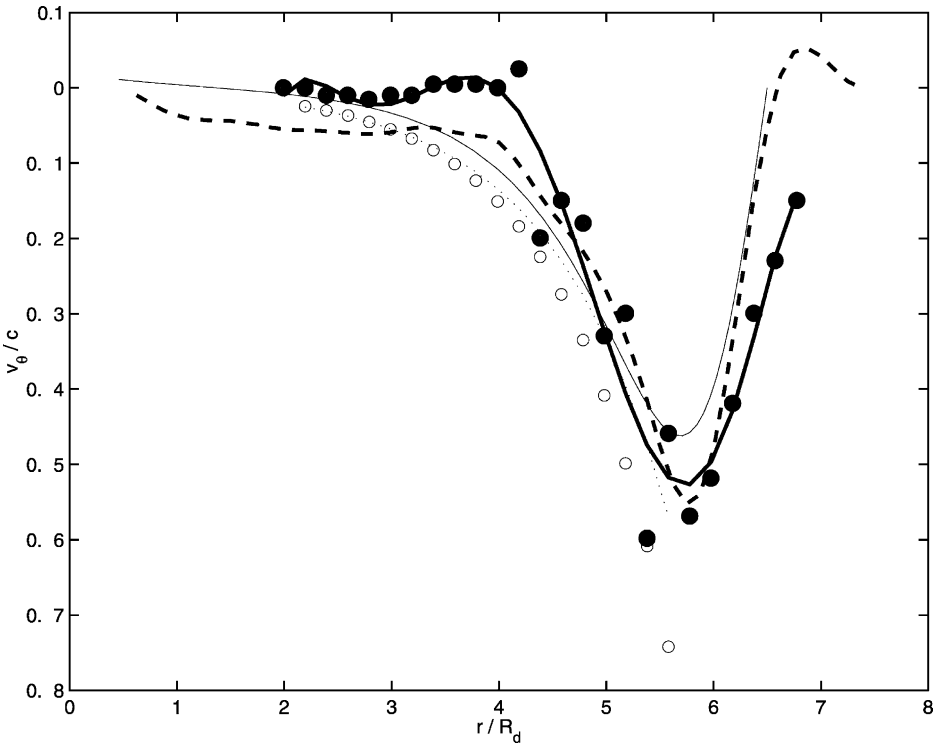

Fig. 6. Radial profile of the mean azimuthal velocity (compared to the phase speed of internal gravity waves) at time $t \sim 1.8T$ for $W^2 = 3.96$, $\delta = 1$, $f = 2.0$ rad/s (Exp3). Experimental points are represented with filled circles while the thick continuous line is the fitted profile of the experimental points. Theoretical profiles obtained by Griffiths and Linden (1982) (small circles), Csanady (1979) (thin dotted line) and by Flierl (1979) (thin continuous line) are plotted as well. The mean profile obtained in numerical simulations (see II) (with same W^2, δ and f) is shown for comparison (thick dotted line).

potential vorticity and geostrophy in a rectangular geometry. The surface velocity has an hyperbolic sine shape with the maximum value at the edge of the front (Griffiths and Linden, 1982). Another model including the effects of cylindrical geometry, which was proposed by Csanady (1979), is also shown in this model. However, this model can not describe the velocity when the upper layer vanishes since the centrifugal force is not taken into account (Flierl, 1979). This explains why this model only differs slightly from that by Griffiths and Linden (1982). Instead our results are in closer agreement with the model proposed by Flierl (1979). This model, which allows an outcropping interface, derives the azimuthal velocity from the equations of motion assuming potential vorticity conservation. Flierl's model gives a profile very similar to that obtained experimentally. The width of the shear region is of about 3Rd which is in very close agreement to our results (Fig. 7) although mixing effects are not taken into account in this model.

The influence of the coast is shown in Fig. 7a, which plots the maximum velocity of the adjusted front, and in Fig. 7b, which shows the typical width of the shear region, as functions

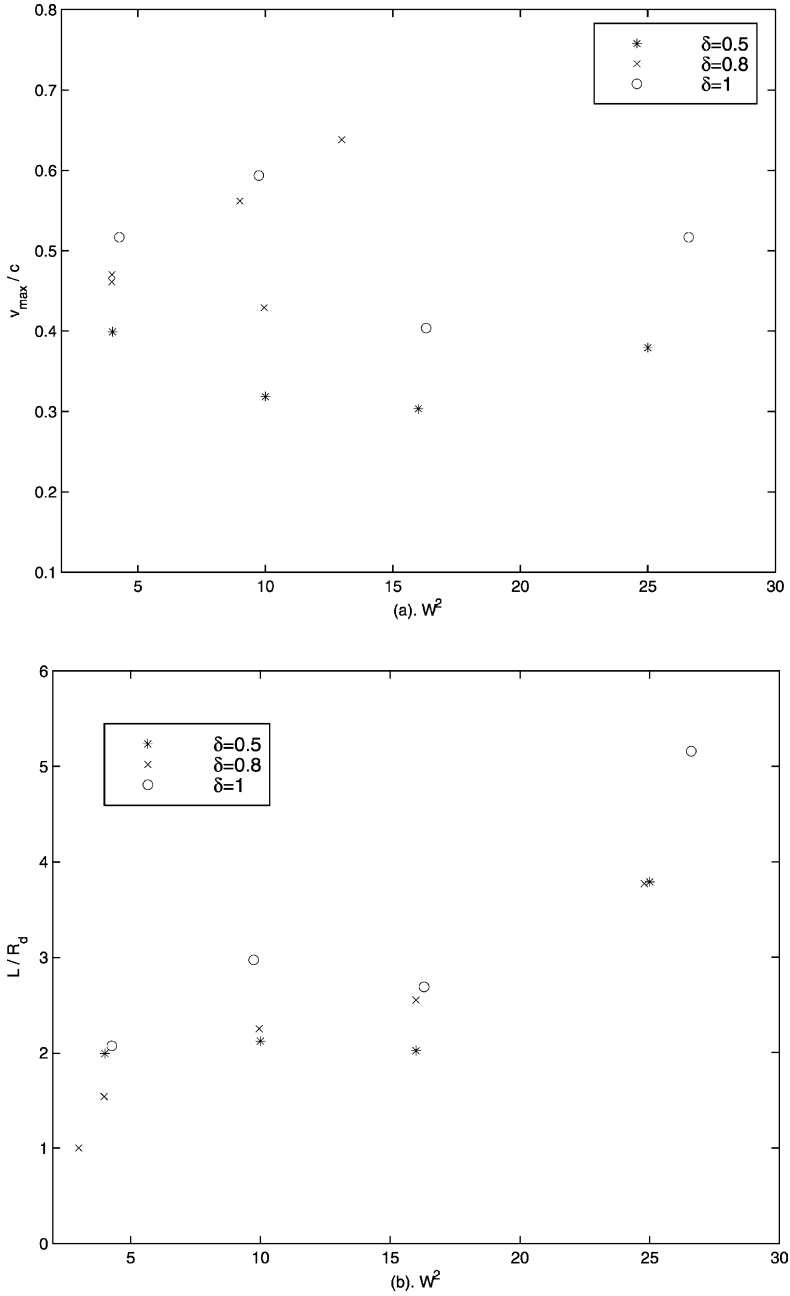

Fig. 7. (a) Maximum velocity of the adjusted front compared to internal wave phase speed as a function of W^2. (b) Typical width of the shear of the adjusted front as a function of W^2. Symbols correspond to different values of the depth ratio: $\delta = 1$ (circles), $\delta = 0.8$ (crosses), $\delta = 0.5$ (stars).

of W^2. The width of the shear region is inferred from the ratio between the maximum velocity and the minimum value of the vorticity. Maximum velocities are found within the range $[0.3(g'h)^{1/2}$ to $0.5(g'h)^{1/2}]$ independent of the value of W^2 (Fig. 7a). In contrast, the typical width of the shear region decreases with W^2 (Fig. 7b), consistent with the maximum value of the anticyclonic vorticity increasing with decreasing W^2.

4.2. Instability of the front and eddy structures

The wavelength is evaluated from the number n of crests and by assuming that the patch spreads over a distance equal to the radius of deformation as inferred from the following expression: $\lambda = 2\pi\ (R_0 + \mathrm{Rd})/n$. We first compare our results with those of Chia et al. (1982) in Fig. 8a in which the wavelength is displayed as a function of W^2. We also find that the wavelength of the perturbation scales like the geometric mean of the radii of deformation of the two layers (see also Fig. 8b): $\lambda/(2\pi \mathrm{Rd}_{\mathrm{mean}}) = 1.08$. This value of 1.08 is close to that of 1.16 value obtained by Chia et al. (1982). Our value is equal to the theoretical value of 1.08 inferred from the two-layer quasi-geostrophic model (Phillips, 1954)) and is close to the 1.15 value obtained by Killworth et al. (1984). Our results show that the wavelength does not depend upon the distance between the front and the boundary and this is consistent with the fact that the instability first develops away from the boundary.

Growth rates of the instability are inferred from the time evolution of the vorticity. The time evolutions of the spatially averaged cyclonic and anticyclonic vorticity are displayed in Fig. 9. The front starts to become unstable after about three rotation periods and an exponential growth is observed during four rotation periods: cyclonic vorticity is growing at the wave troughs while anticyclonic vorticity is decreasing at the wave crests. The growth rate of the cyclonic vorticity is slightly higher than that of the anticyclonic vorticity (following the process described in Section 4.1). The instability then saturates when the cyclonic eddies are advected across the front ($t \sim 7T$).

The growth rate of the instability varies with W and δ. Fig. 10, in which the growth rate is represented versus the depth ratio for three values of W, summarizes these two evolutions. The theoretical growth rate obtained from the analogue of Phillips's model but in a cylindrical geometry following Holford (1994) and Holford and Dalziel (1996) is shown for comparison. Calculations of the most unstable wavelength and its growth rate are detailed in Holford (1994). The theoretical growth rate first increases with δ and then decreases for $\delta > 0.7$. For fairly high values of W, ($W^2 \sim 25$, Fig. 10a) the growth rate first increases with δ and slightly decreases for $\delta \gtrsim 0.7$. This evolution is in good agreement with theory, especially for the anticyclonic vorticity, suggesting that ageostrophic effects occurring at the front do not affect crucially the growth of the instability (Fig. 10a). For smaller values of W ($W^2 \sim 9$ and $W^2 \sim 4$), the growth rate increases with δ (Fig. 10b and c). The scatter of the experimental results comes from slight variations in W^2 and δ (see captions of Fig. 11b and c). The growth rate increases with decreasing W^2, corresponding to an increasing amount of potential energy released.

For small W the theoretical growth rate only describes the experimental evolution qualitatively (Fig. 10c). One reason for this discrepancy is the increasing effect of the boundaries as the radius of deformation increases.

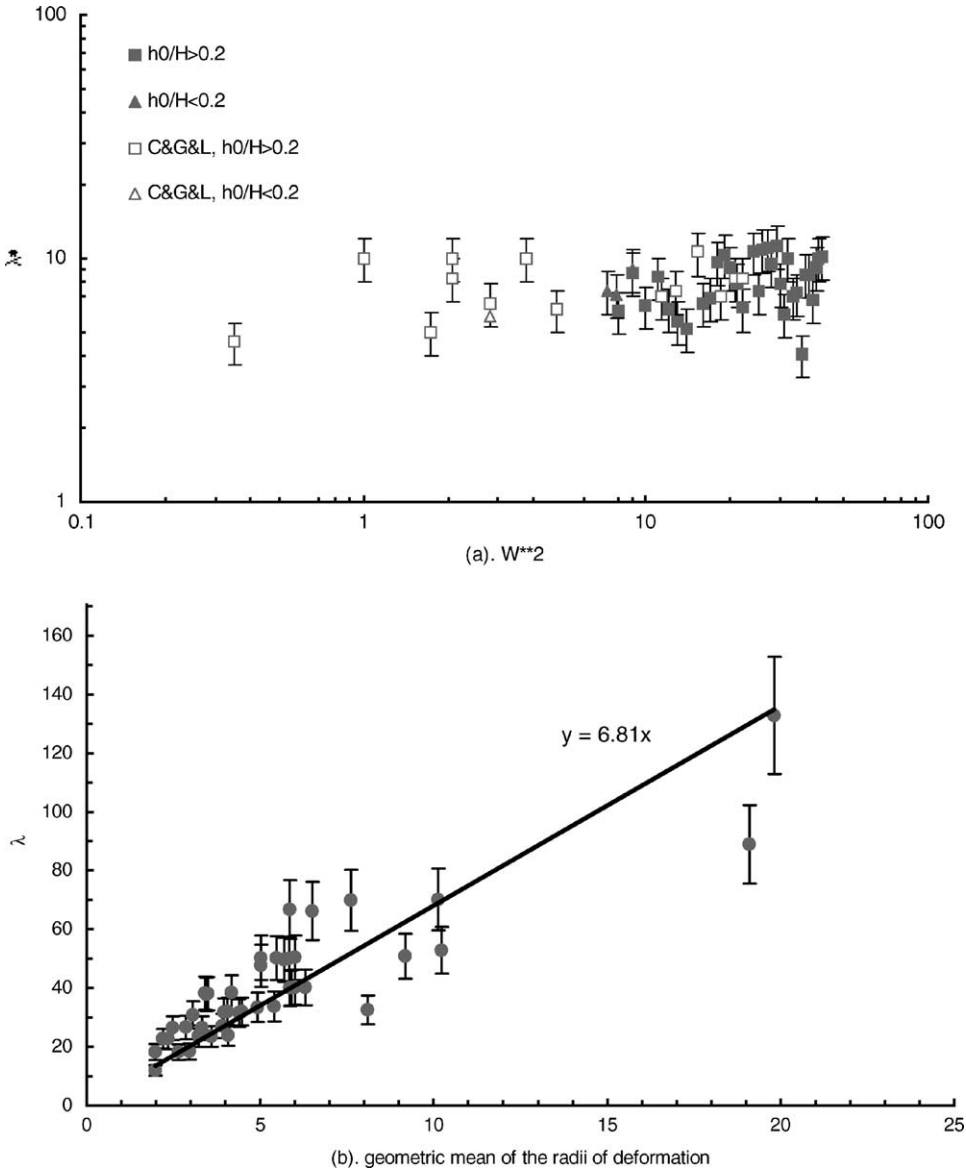

Fig. 8. (a) Nondimensionalized wavelength (relative to the geometric mean of the radii of deformation of the two layers) vs. $W^2 = (L/\mathrm{Rd})^2$. The experimental values obtained by Chia et al. (1982), denoted as (C&G&L) are represented as well. (b) Wavelength as a function of the geometric mean of the radii of deformation of the two layers. The wavelength is inferred from the number of wave crests (n) following: $\lambda = 2\pi\ (R_0 + \mathrm{Rd})/n$. The error mostly results from the estimate of n and is of the order of 20%.

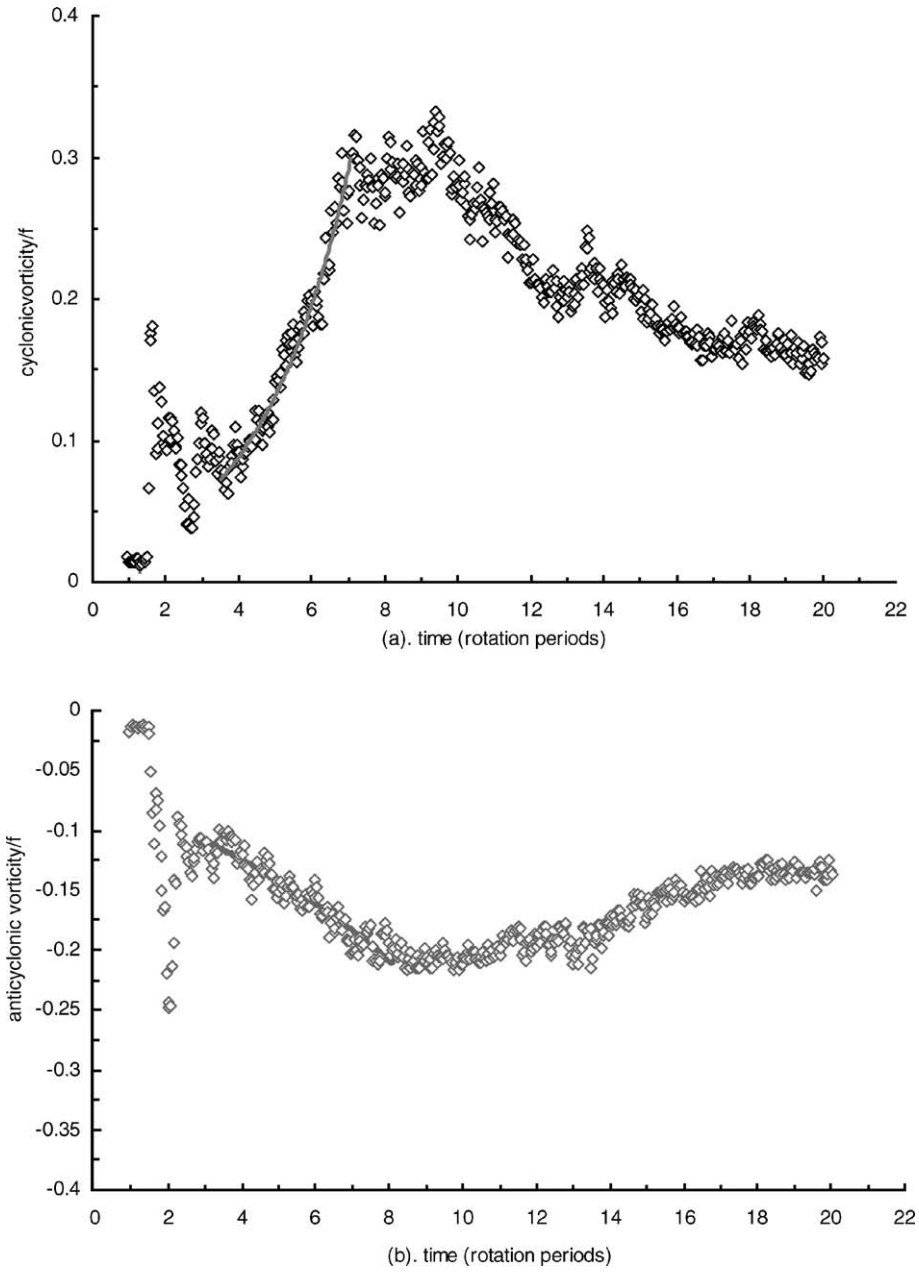

Fig. 9. Growth of the instability. (a): Spatially averaged cyclonic vorticity relative to the inertial frequency as a function of time (rotation periods) for $W^2 = 3.96$, $\delta = 1$, $f = 2.0$ rad/s (Exp3). The growth starts at $t \sim 3.5T$ and saturates at $t \sim 7T$. The growth rate is inferred from the exponential fit which is represented with a thick black line. (b): Spatially averaged anticyclonic vorticity relative to the inertial frequency as a function of time (Exp3).

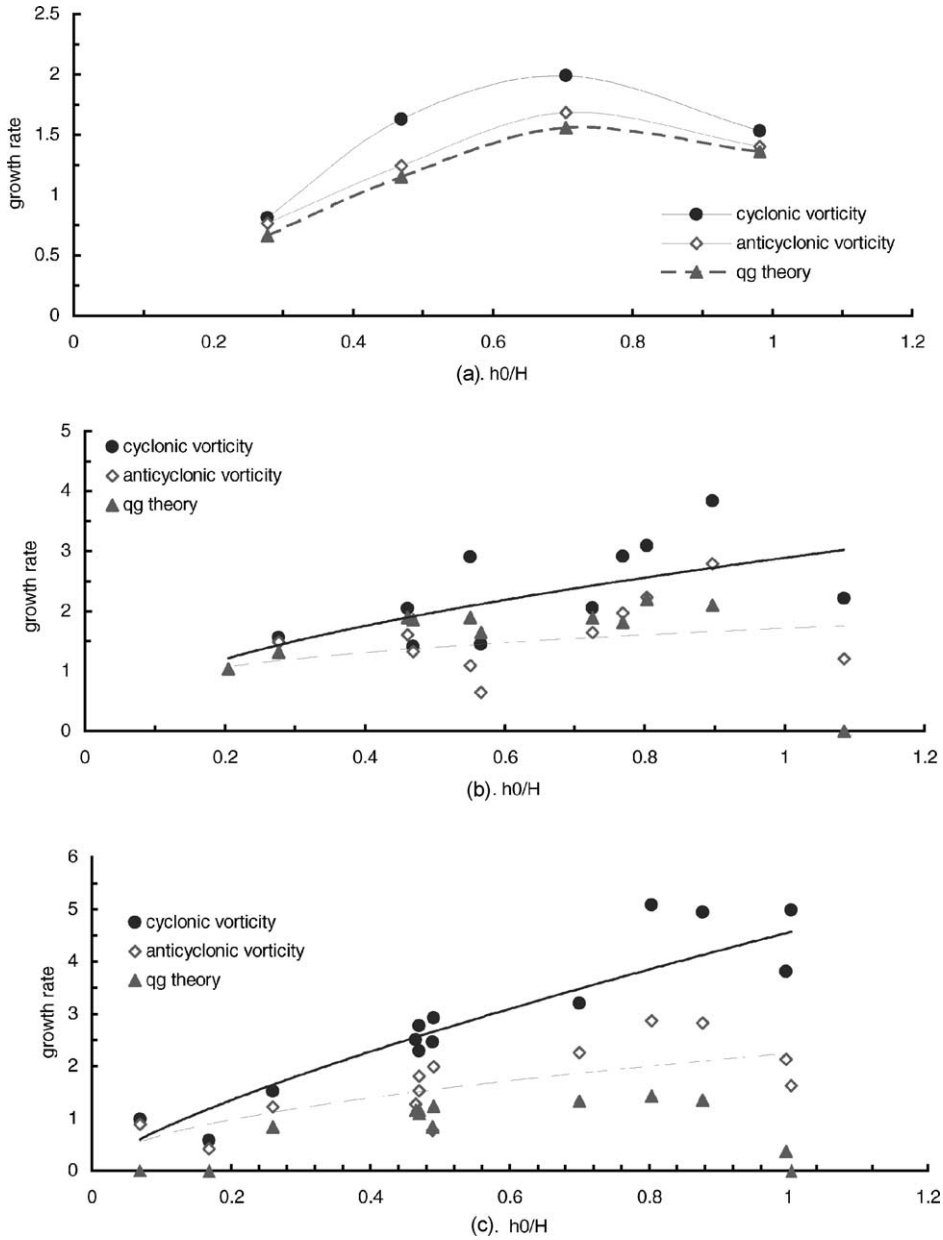

Fig. 10. Growth rate of the averaged cyclonic and anticyclonic vorticity as a function of the depth ratio for three values of W^2, the growth rate obtained from quasi-geostrophic theory (see text) is represented as well for comparison (a): W^2 ∼(25.5–27); (b): W^2 ∼(7.9–10); (c): W^2 ∼(3.9–5.8).

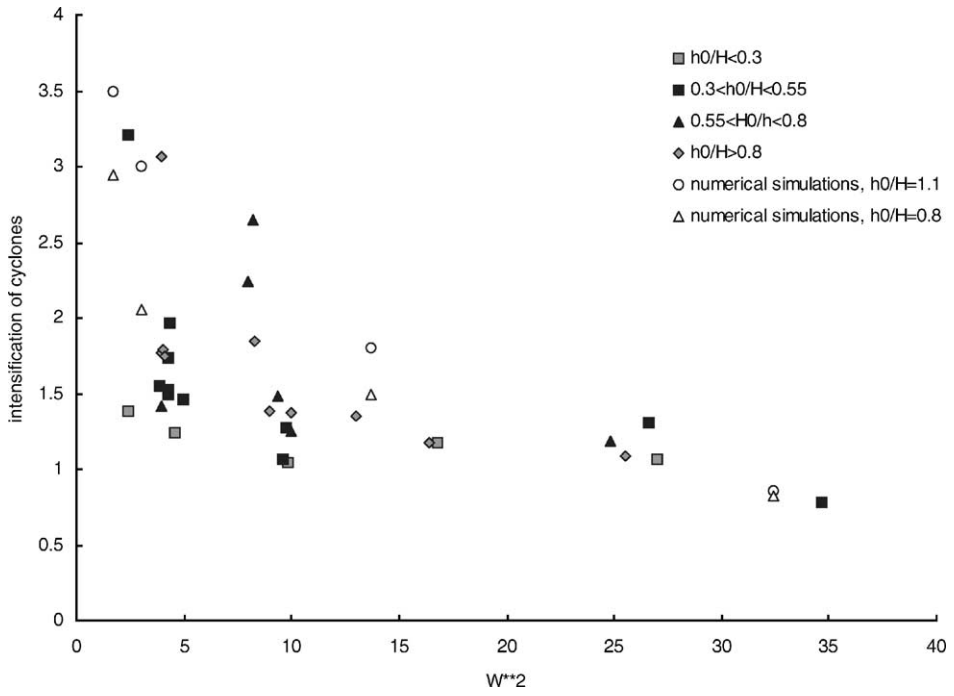

Fig. 11. Intensification of cyclonic eddies: ratio between the growth rate of the averaged cyclonic vorticity and that of the averaged anticyclonic vorticity as a function of W^2. Numerical results obtained in II are shown for comparison.

The striking effect of the coast is to enhance the growth of cyclonic eddies as opposed to that of the anticyclonic vorticity. This effect, which was previously observed by Chia et al. (1982), is described quantitatively here. The intensification of cyclonic eddies, defined as the ratio between the growth rates of cyclonic and anticyclonic vorticity, is displayed as a function of W^2 in Fig. 11. Numerical results obtained by II are also plotted in Fig. 11. Excellent agreement is obtained between the two approaches. The intensification increases from unity for $W^2 \sim 25$ and reaches a value of about 3.5 for $W^2 \sim 2.5$. This intensification mainly results from the baroclinic wave separation at the coast as previously described. In addition higher intensification is observed for increasing depth ratio ($\delta > 0.55$) in both the laboratory experiments and the numerical simulations. Presumably, the lower layer flow, which is more intense for increasing δ, contributes more efficiently to the enhancement of cyclonic eddies.

5. Conclusion

We investigated experimentally the evolution of a front in a two-layer stratification and with background rotation. The experiments focused on the influence of the boundary upon the adjustment and the subsequent instability of the front.

The experiments were a replication of those performed by Chia et al. (1982) but here a quantitative analysis based upon surface velocity and vorticity fields was made possible with new measurement techniques (particle tracking). The front was produced through the adjustment of a buoyant patch of fluid: an anticyclonic motion develops in the buoyant fluid while a ring of cyclonic vorticity around the edge of the front arises as a result of shear instability and subsequent mixing. The front is then unstable to azimuthal waves whose growth mainly results from baroclinic processes. At large amplitude, cyclonic eddies form at the wave troughs and they eventually entrain the anticyclonic crests of the waves. We found that the effect of the boundary is crucial with respect to the instability of the front and leads to the enhancement of cyclonic eddies consisting of "coastal" waters. The growth rate of the instability mostly depends upon two parameters, W and δ, where W is defined as the width of the upwelling region in units of the internal radius of deformation while δ is the depth ratio between the two layers. For the highest values of W ($W^2 \sim 25$), when the instability takes place "far" from the boundary, the growth rate of the instability is in close agreement with that provided by a two-layer quasi-geostrophic model for baroclinic instability in a cylindrical geometry. For decreasing values of W^2 ($W^2 < 16$), the growth rate of cyclonic vorticity is enhanced compared to that of anticyclonic vorticity. We found that the intensification of cyclonic eddies is increasing with decreasing W^2. As well the intensification is stronger for higher depth ratio and barotropic processes for the lower layer fluid might contribute to this process. It would be interesting to track eddies and estimate the vorticity during the onset and later evolution of the instability of oceanic upwelling fronts which fall into our W^2 range (1.5–16). For instance, we found a few cases in the ocean or lakes for which cyclonic eddies could be intensified: the upwelling off the coast of California ($W^2 \sim 9$, inferred from Flament et al. (1985)), the Benguela upwelling ($W^2 \sim 7$, inferred from Penven et al. (2001)), the upwelling in lake Ontario ($W^2 \sim 1$ inferred from Csanady (1977)).

The effect of the coast on the eddy growth will have a significant impact on exchanges across the front. Once cyclonic eddies have been enhanced at the coast they are ultimately advected off-shore across the front. This occurs typically for $W^2 \sim 16$. We can thus estimate from the number n of cyclonic eddies and their diameter, the coastal water volume advected across the front. This coastal water volume compared to the buoyant water volume varies like $n(\mathrm{Rd}/R_c)^2\,(H/h_0)$. Thus a higher volume of coastal water is advected off-shore when the front develops closer to the coast. Note that here since the upwelling is not forced we consider the coastal water volume advected off-shore. Another way would be to perform forced experiments and to characterise the rate of off-shore coastal water advection. Also it could be interesting to keep the same n and Rd value but to vary the size of the tank. In this way, the water volume of cyclonic eddies would be the same whatever the value of W^2. Eventually since the vorticity of the cyclonic eddies is greater for near-coast front, it is likely that these structures will have a greater fertilising effect since their lifetime will be increased.

Also it would be relevant to investigate the influence of bottom topography on eddy growth and later evolution of the front: Reszka and Swaters (1999) showed that baroclinic instability is hindered when the interface slopes in the same sense as the slope. Preliminary laboratory experiments suggest that cyclonic eddies then remain in the sloping region (Bouruet-Aubertot and Linden, 1999) which might have consequences on exchanges.

Acknowledgements

The authors wish to thank D. Lipman, B.L. Dean, D. Page-Croft for technical support during the laboratory work and J. Hacker and J.M. Holford for helpful discussions. P.B.A. acknowledges the support of a grant from the European Community (ERBFMBICT972486).

References

Bouruet-Aubertot, P., Echevin, V., 2002. The influence of the coast on the dynamics of upwelling fronts. Part II: Numerical experiments. Dyn. Atmos. Oceans 36 (1–3), 175–200.

Bouruet-Aubertot, P., Linden, P.F. Laboratory experiments on upwelling fronts. In: Proceedings of the Communication at the EGS Meeting, Den Haag, April 1999.

Cenedese, C., 1998. Baroclinic eddies over topography. Ph.D. Thesis. DAMTP, Cambridge University, Cambridge.

Chia, F., Griffiths, R.W., Linden, P.F., 1982. Laboratory experiments on fronts. Part 2. The formation of cyclonic eddies at upwelling fronts. Geophys. Astrophys. Fluid Dyn. 19, 189–206.

Crépon, M., Wald, L., Monget, J.M., 1982. Low frequency waves in the Ligurian Sea during December 1977. J. Geophys. Res. 87 (C1), 595–600.

Csanady, G.T., 1977. Intermittent full upwelling in lake Ontario. J. Geophys. Res. 82, 397–419.

Csanady, G.T., 1979. The birth and death of a warm core ring. J. Geophys. Res. 84, 778–780.

Cushman-Roisin, B., Heil W.H., Nof, D., 1985. Oscillations and rotations of elliptical warm-core rings. J. Geophys. Res. 90 (C6), 11756–11764.

Dalziel, S.B., 1992. DigImage: System Overview. Cambridge Environmental Research Consultants Ltd., p. 43.

Flament, P., Armi, L., Washburn, L., 1985. The evolving structure of an upwelling filament. J. Geophys. Res. 90 (C6), 11765–11778.

Flierl, G.R., 1979. A simple model for the structure of warm and cold core rings. J. Geophys. Res. 84, 781–785.

Gill, A.E., 1982. Atmosphere–Ocean Dynamics Inc., p. 662.

Gill, A.E., Green, J.S.A., Simmons, A.J., 1974. Energy partition in the large-scale ocean circulation and the production of mid-ocean eddies. Deep Sea Res. 21, 499–528.

Griffiths, R.W., Linden, P.F., 1981a. The stability of vortices in a rotating, stratified fluid. J. Fluid Mech. 105, 283–316.

Griffiths, R.W., Linden, P.F., 1981b. The stability of buoyancy-driven coastal currents. Dyn. Atmos. Oceans 5, 281–306.

Griffiths, R.W., Linden, P.F., 1982. Laboratory experiments on fronts. Part 1. Density-driven boundary currents. Geophys. Astrophys. Fluid Dyn. 19, 159–187.

Holford, J.M., 1994. The evolution of a front, Ph.D. Thesis. DAMTP, Cambridge University, Cambridge.

Holford, J.M., Dalziel, S.B., 1996. Measurements of layer depth during baroclinic instability of a two-layer flow. Appl. Sci. Res. 56, 191–207.

Ikeda, M., Emery, W.J., 1984. Satellite observations and modelling of meanders in the California current system off Oregon and northern California. J. Phys. Oceanogr. 14, 1434–1450.

Killworth, P.D., Paldor, N., Stern, M.E., 1984. Wave propagation and growth on a surface front in a two-layer geostrophic current. J. Marine Res. 42, 761–785.

Kunze, E., 1985. Near-inertial wave propagation in geostrophic shear. J. Phys. Oceanogr. 15, 544–565.

Linden, P.F., 1991. Dynamics of fronts and eddies. Proceedings of Enrico Fermi Summer School on “Non linear topics in Ocean Physics”, Ed. A. Osborn. North Holland, pp. 313–351.

Linden, P.F., Boubnov, B.M., Dalziel, S.B., 1995. Source-sink turbulence in a rotating stratified fluid. J. Fluid Mech. 298, 81–112.

F Pearce, A., Griffiths, R.W., 1991. The mesoscale structure of the Leeuwin current: a comparison of laboratory models and satellite imagery. J. Geophys. Res. 96 (C9), 16739–16757.

Penven, P., Lutjeharms, J.R.E., Marchesiello, P., Roy, C., Weeks, S.J., 2001. Generation of cyclonic eddies by the algulhas in the lee of the algulhas bank. Geophys. Res. Lett. 28 (6), 1055–1058.

Phillips, N.A., 1954. Energy transformations and meridional circulations associated with simple baroclinic waves in a two-level, quasi-geostrophic model. Tellus 6, 273–286.

Ramp, S.R., Jessen, P.F., Brink, K.H., Niller, P.P., Dagget, F.L., Best, J.S., 1991. The physical structure of cold filaments near point Arena, California, during June 1987. J. Geophys. Res. 96 (C8), 14859–14883.

Reszka, M.K., Swaters, G.E., 1999. Eddy formation and interaction in a baroclinic frontal geostrophic model. J. Phys. Oceanogr. 29, 3025–3042.

Strub, P.T., Kosro, P.M., Huyer, A., 1991. The nature of the cold filaments in the Californian current system. J. Geophys. Res. 96 (C8), 14743–14768.

Verzicco, R., Lali, F., Campana, E., 1997. Dynamics of baroclinic vortices in a rotating stratified fluid: a numerical study. Phys. Fluids 9 (2), 419–432.